machines

MDPI

Article

Simulation Study on the Evolution Behaviour of Endogenous Third Bodies in the Rough Friction Interface During Braking and Their Impact

Lu Jin [1], Shengfang Zhang [1], Guotao Ru [2], Jian Yin [1], Li Shi [1], Xin Li [1], Zhihua Sha [1] and Yu Liu [1,*]

[1] School of Mechanical Engineering, Dalian Jiaotong University, Dalian 116028, China; jinlu0807@163.com (L.J.); zsf_djtu@163.com (S.Z.); yj15241486995@163.com (J.Y.); li_shi1997@foxmail.com (L.S.); romantic.li.x@gmail.com (X.L.); zhsha_djtu@163.com (Z.S.)

[2] Xi'an Railway Signal Co., Ltd., Xi'an 710104, China; rtt1048759201@163.com

* Correspondence: liuyu_ly12@126.com

Abstract: During braking, high-power wind turbine disc brake friction pairs experience thermo-mechanical interactions at the interface, which lead to both physical and chemical changes. The friction interface features asperities and embedded hard particles within the substrate. Wear debris from these asperities or dislodged hard particles accumulates at the interface, continuing to participate in the friction process—a phenomenon known as the "endogenous third body". Throughout braking, the microscopic morphology and contact conditions of the interface evolve dynamically. The stress–strain distribution and vibration behaviour of the friction system, influenced by the endogenous third body, also vary with braking parameters. This study employs the W-M fractal theory to develop a finite element model of a rough friction interface containing hard-particle endogenous third bodies. The model is validated through experimental testing. Based on the performance test parameters of high-power wind turbine disc brakes, a simulation is conducted to analyse the contact friction process involving the endogenous third body at the rough interface between the brake disc and brake pad. The simulation reproduces the formation process of the endogenous third body and reveals its evolutionary stages, including "ploughing", "gap-filling", and "aggregation". Additionally, the study examines changes in the internal stress–strain and vibration states of the friction system under varying braking speeds (5 m/s to 35 m/s) and braking loads (3 MPa to 6 MPa). The findings demonstrate how different braking parameters influence the friction system containing the endogenous third body. The results showed that when the braking speeds were 5 m/s, 15 m/s, 25 m/s, and 35 m/s, and the braking load was 6 MPa, the average amplitude of the brake pads was the smallest, at 0.017 mm, 0.021 mm, 0.025 mm, and 0.020 mm, respectively. This research provides valuable insights into the three-body contact friction mechanism at the micro-braking interface, the formation of composite material third bodies, and the role of wear-stage third bodies in affecting the friction interface.

Keywords: friction interface; endogenous third body; evolutionary behaviour

check for updates

Academic Editor: Sheng Li

Received: 23 December 2024
Revised: 8 January 2025
Accepted: 21 January 2025
Published: 23 January 2025

Citation: Jin, L.; Zhang, S.; Ru, G.; Yin, J.; Shi, L.; Li, X.; Sha, Z.; Liu, Y. Simulation Study on the Evolution Behaviour of Endogenous Third Bodies in the Rough Friction Interface During Braking and Their Impact. *Machines* **2025**, *13*, 83. https://doi.org/10.3390/machines13020083

Copyright: © 2025 by the authors. Licensee MDPI, Basel, Switzerland. This article is an open access article distributed under the terms and conditions of the Creative Commons Attribution (CC BY) license (https://creativecommons.org/licenses/by/4.0/).

1. Introduction

Wind power is crucial to the future energy supply. Fueled by the "dual carbon" objectives, the global demand for wind energy is rising. By 2030, the European Union is expected to increase its share of renewable electricity generation to over 40%, while China is projected to contribute 20% [1,2] of the global installed capacity. Currently, China is the

world's largest manufacturing hub for wind power equipment. To ensure the high-quality development of the wind energy sector in the future, it is imperative to further reduce the levelized cost of electricity (LCOE) and lessen the dependence on the importation of key components [3,4]. Scaling up wind turbines is one of the primary strategies to reduce LCOE. As the trend towards larger turbines accelerates, the reliability of core components becomes increasingly crucial to the operation of wind turbines. Consequently, it is vital to focus on advancing the core technologies of these components to enhance the safety, reliability, and overall performance of wind power equipment, thus facilitating the transition to a green, low-carbon energy system. Disc brakes, which are vital for ensuring the safe operation of high-power wind turbines, experience frictional wear on the rough contact interfaces between the brake disc and brake pad during braking, which compromises the operational safety of wind turbines. Typically, brake pads are made of copper-based powder metallurgy materials, with the matrix containing hard-particle friction components. When subjected to the combined effects of force and heat, wear occurs, causing the hard particles to detach from the matrix and remain within the friction interface gap. These particles then contribute to the friction process and affect the vibration of the braking system, significantly impacting braking performance.

Research on the friction and wear characteristics of braking system interfaces often assumes a static morphology for the braking interface, disregarding the impact of wear and frictional processes during operation. Such investigations frequently rely on idealised models [5]. In real-world braking scenarios, the interactions between friction pairs generate thermo-mechanical effects at the interface, resulting in both physical and chemical transformations. These changes include alterations in elemental distribution, plastic deformation, material removal, material transfer, and wear. Idealised models classify the materials of the braking interface as the first and second bodies, forming a two-body friction system. However, wear particles generated during braking which are retained at the interface, or foreign materials introduced into the interface, create a "third body" that actively participates in the friction process, thus converting the system into a three-body friction system [6]. Wear particles originating from interface materials are termed endogenous third bodies, while externally introduced materials are referred to as exogenous third bodies. Since wear and friction are unavoidable during braking, three-body systems—especially those incorporating endogenous third bodies—represent real braking conditions more accurately and hold significant research value. The transition from a two-body to a three-body friction system, driven by the formation of third bodies, has led to extensive research into their formation mechanisms and evolutionary dynamics. Godet first introduced the concept of the third body in 1984, defining it as a distinct region in the friction system with material properties different from those of the first and second bodies [7]. Since then, numerous studies have explored the role of third bodies in braking interface systems.

In the research of the effects of various third-body types on friction performance, Du X [8] developed a precise system for introducing exogenous copper-powder third bodies, analysing their impact on diverse copper-based friction materials. Su L [9] used a pin-on-disc tribometer to examine the influence of prefabricated iron-powder third bodies on the frictional performance of copper-based composites. Linlin S [10] extended this work by analysing the relationships between the composition, friction coefficients, and surface morphology of copper–iron third bodies through the addition of copper and iron powders. Yang H [11] compared the wear rates and friction coefficients of C/C-SiC composites with and without exogenous third bodies, elucidating the tribological effects of various exogenous compositions. Chun T [12] examined adhesion coefficients under different third-body mediums in wheel–rail systems, proposing strategies to optimise adhesion for enhanced traction, braking efficiency, and safety. V. D. G [13] investigated the effects of

environmental contaminants, such as leaves, clay, and iron oxides, on adhesion under wet conditions using a twin-disc tester. Stefan F [14] evaluated the frictional behaviour of three distinct C/C–SiC third-body materials.

In the research on surface morphology changes in friction pairs, Ahmed S. K [15] introduced a novel friction measurement device to assess third-body-induced damage on wheel–rail interfaces. Simone C [16] proposed an experimental method to evaluate the effects of third bodies on contact surfaces under dry friction conditions. Pierre A [17] developed a predictive wear model incorporating third-body debris layers and adhesive wear, focusing on the distribution of frictional energy. Manqi Y [18] studied the effects of third-body composition on brake disc temperatures by introducing third bodies into braking interfaces. Xiaoyu Y [19] designed a conveyor belt-driven spring–block system to analyse the dynamic effects of third-body intrusion on friction forces. Singla N [20] used a simplified test rig with a transparent glass disc and artificial alumina third bodies to study the relationship between third-body layer changes and the onset of squealing in dry sliding conditions. Irina G [21] modelled third-body effects on rolling contact fatigue, investigating the stress distribution and crack initiation influenced by longitudinal slip, friction coefficients, and intermediate layer properties. Olivier B [22] simulated third-body damage on contact surfaces, quantifying stress concentrations and wear patterns. Zhao F [23] studied coatings' effects on friction and wear, analyzing surface roughness, wear track hardness, friction coefficients, and wear rates. Joaquin S. G [24] simulated the evolution of surface roughness during third-body-mediated friction processes using molecular dynamics.

In the research of fretting wear, Soha B [25] explored the influence of third bodies on fretting wear rates using the third-body theory. Mi X [26] examined the role of third bodies in the fretting wear of 690 alloys. Zhu T [27] proposed a relationship between maximum wear rates and contact dimensions during debris discharge in fretting wear. Liskiewicz T [28] investigated how engineered metal interfaces can reduce contact resistance and extend the service life of automotive connectors under third-body fretting conditions. Shengzan Z [29] analysed the impact of temperature on third-body layer formation and its effect on fretting wear in surface materials. Arman A [30] created a finite element model to simulate third-body behaviour in fretting wear, assessing the influence of particle characteristics, including elastic modulus, yield strength, and particle count, on contact stress and stick–slip phenomena.

In the research of third-body evolution, Zhou Y [31] examined third-body and crack behaviour in pearlitic steel during friction testing. He Y [32] measured friction and conductivity during sliding tests on graphite, identifying the morphological evolution of nano-scale third-body layers. Yan X [33,34] used FEM-DEM coupling methods to model third-body behaviour at friction interfaces, analysing nonlinear phenomena and demonstrating how third-body particles induce instability by monitoring stress and displacement. Son B. P [35] simulated adhesive wear using discrete element methods, studying the effects of material properties and load parameters on third-body layer performance during sliding. I. I. A [36] employed continuum mechanics to model fretting wear, analysing variations in third-body layer profiles, thickness, and volume under rough surface contact. The research on third bodies at braking interfaces primarily focuses on their influence on friction performance, surface morphology changes, fretting wear, and evolutionary processes. However, studies on the generation and evolution of third bodies, particularly endogenous ones, remain limited.

This study concentrates on endogenous third bodies, which are formed from wear debris or dislodged hard particles embedded in the substrate of the friction interface. These particles remain at the interface and continue to influence the friction process. A

finite element model of a rough friction interface containing endogenous third bodies is developed using W-M fractal theory to characterise the asperity features of the braking interface. The model simulates the contact friction process involving endogenous third bodies at the rough interface between the brake disc and brake pad and is validated through experimental testing.

The existing model is simplified based on the following assumptions:

(1) Inertial forces across the entire friction system are disregarded.
(2) As the model is two-dimensional and incapable of simulating heat dissipation, temperature variations in the frictional environment are excluded.
(3) Third-body particles participating in the friction process are considered homogeneous aggregates of SiO_2, possessing uniform diameters and spherical shapes.
(4) All contacts within the friction system adhere to Coulomb friction, with a constant friction coefficient applied.

2. Finite Element Model of an Endogenous Third-Body Friction System

This study defines the simulation parameters for the finite element model based on the actual operating conditions and performance test data of high-power wind turbine disc brakes. The operating conditions primarily differ in two braking parameters: braking speed and braking load. By integrating the profile parameters of the braking interface and the size of third-body particles, the study establishes a range of braking parameters for the three-body friction process. These parameters provide a theoretical basis for determining the boundary conditions and load settings in subsequent simulation analyses.

As shown in Figure 1, during the braking process of a disc brake, the brake disc rotates at a speed of n in a predetermined direction. Simultaneously, the brake pad is pushed by the braking load, pressing firmly against the brake disc.

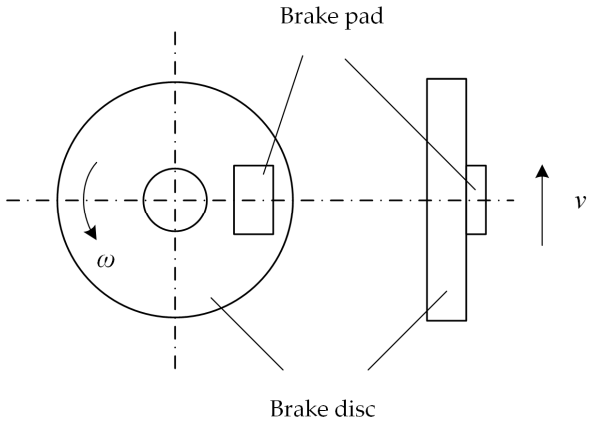


Figure 1. Main motion model of disc brake.

Table 1 provides the recommended performance test parameters for high-power wind turbine disc brakes, as outlined in the Energy Industry Standards of the People's Republic of China: Hydraulic Disc Brakes for High-Speed Shafts of Wind Turbines. The standard specifies that the rotational speed of the brake disc during braking should range between 80 and 1000 r/min, with the emergency braking speed set at 1000 r/min. Using the primary motion model of the disc brake during braking, these recommended performance test parameters are converted into the equivalent data. Assuming a braking radius of 300 mm, the relationship between the relative sliding speed (v) of the brake disc and pad and the rotational speed (n) of the brake disc is expressed as follows:

$$v = \frac{2\pi r}{60} n \tag{1}$$

Table 1. Recommended parameters for performance test of disc brake.

Project	Recommended Parameters	Equivalent Conversion Parameters
Brake disc radius R (mm)	400	400
Braking radius r (mm)	300	300
Emergency braking initial speed	1000 (r/min)	31.4 (m/s)

In Equation (1), r represents the braking radius, n indicates the rotational speed of the brake disc, and v denotes the relative sliding speed of the brake pad. Utilising Equation (1) along with the recommended test parameters, the calculated range for the relative sliding speed between the brake disc and the brake pad is 2.5 to 31.4 m/s.

The braking process of high-power wind turbine disc brakes occurs under high-speed and heavy-load conditions. Under braking pressure, the brake disc and pad surfaces establish close contact, with numerous asperities on the friction interface collectively supporting the mechanical load. As shown in Figure 2, during braking, these asperities dissipate energy through elastic–plastic deformation, material failure, fracture, and frictional interactions. This rapid dissipation of mechanical kinetic energy persists until the braking process is complete. Throughout the process, the microscopic topography and contact state of the rough interface evolve dynamically, with the asperities experiencing continuous changes in stress and strain, alongside fluctuations in the vibration of the entire braking interface.

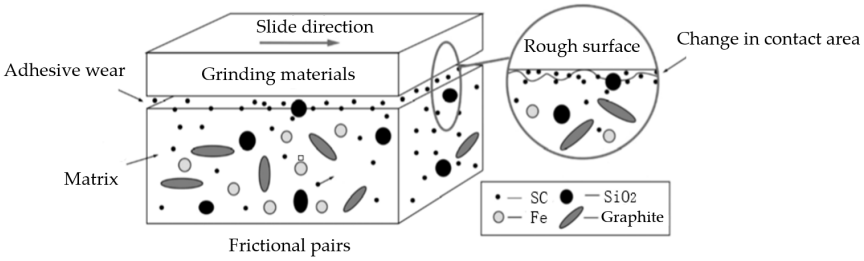


Figure 2. Schematic diagram of the wear of the endogenous third-body friction system.

2.1. The Endogenous Third-Body Model Was Determined

Experimental investigations by Hao Cui [37] demonstrated that during the three-body frictional contact process between the brake disc and pad in high-power braking systems, large granular third-body particles are distributed across the frictional interface. An energy spectrum analysis revealed that these particles primarily consist of SiO_2 and sand, both originating from the brake pad as frictional components (Figure 3). These third-body particles are predominantly spherical, with diameters ranging from 75 to 200 µm. These observations provided the basis for determining the particle size and material properties of the third-body particles incorporated into the finite element model used in this study.

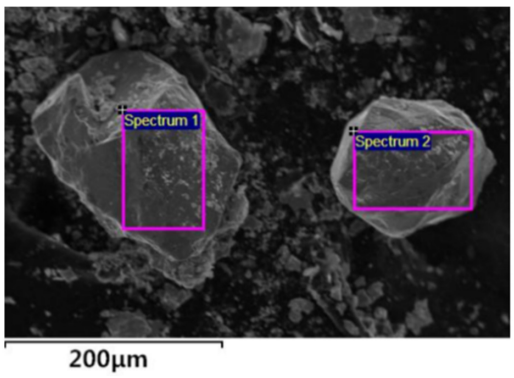


Figure 3. Microscopic morphology of endogenous tertiary body [37].

2.2. A Rough Surface Model Based on W-M Fractal Function Was Established

The W-M fractal function is a typical mathematical function used to represent random profiles, enabling the accurate simulation and construction of random surfaces with fractal characteristics. It is continuous yet non-differentiable. The mathematical model is expressed as follows:

$$Z(x) = G^{(D-1)} \sum_{n=n_1}^{\infty} \gamma^{(D-2)n} \cos(2\pi\gamma^n x) \quad (1 < D < 2, \gamma > 1) \tag{2}$$

In the equation, Z(x) represents the height of the random surface profile, while x denotes the positional coordinate of the profile. The fractal dimension D characterises the irregularity of Z(x) across all scales, whereas G, the characteristic scale coefficient, reflects the magnitude of Z(x) and determines its specific size. The parameter γ denotes the spatial frequency of the profile. For random profiles that follow a normal distribution, γ is typically set to 1.5 to account for the randomness of high-frequency spectral density and phase. Additionally, N represents the natural sequence number, and the scale coefficient G is assigned a fixed value of 0.01.

Based on the W-M fractal theory, fractal curves with specific parameters are simulated using a programming software (ABAQUS2019). The key parameter, the fractal dimension, is derived by converting the measured roughness of the friction surface. A fractal dimension of D = 1.5 is selected to simulate the fractal curves. These curves are subsequently fitted with splines, and a two-dimensional rough surface profile is finally plotted, as shown in Figure 4.

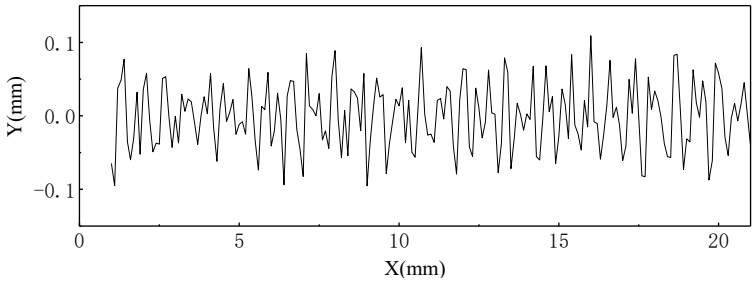


Figure 4. D = 1.5. Two-dimensional rough surface profile topography.

As shown in Figure 5, a contact compression–shear model integrating frictional third-body elements is developed. In this model, the upper rough interface represents the brake pad's friction region, while the lower rough interface corresponds to the brake disc's friction region. The contact surface is populated with asperities of a uniform size and random curvature. The fractal surface is moderately smoothed, and a 0.1 mm load application and velocity application zone is defined on the outer surface of the contact layer. This load-bearing layer, characterised by low density and exceptionally high stiffness to minimise deformation, ensures a uniform force distribution across the upper plate. The geometric dimensions of the model are detailed in Figure 6.

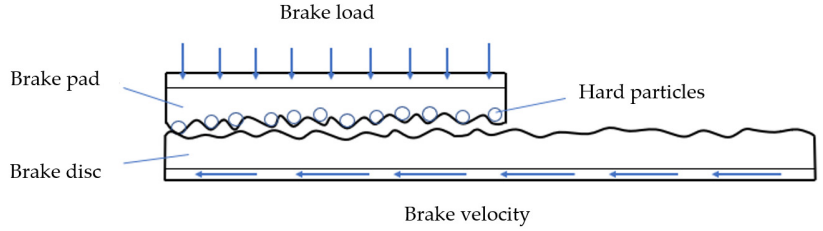


Figure 5. Schematic diagram of the application of the endogenous three-body contact load.

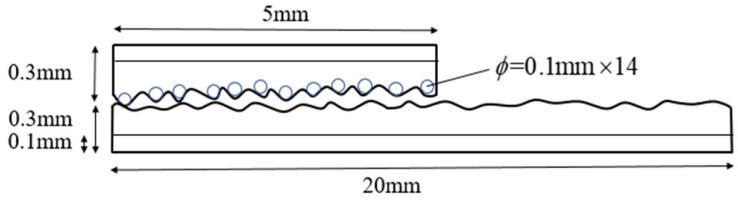


Figure 6. Geometric dimension diagram of internal three-body contact model.

During the three-body contact compression–shear process, friction occurs both between particles and with the contact surface. To simulate these interactions, the model employs a rigid contact framework with "elastic slip" characteristics.

2.3. Material Property Definition and Finite Element Mesh Generation

In the model, the brake pad material is copper-based powder metallurgy, while the brake disc material is Q345B steel. The third-body particles are composed of SiO_2. The detailed material parameters are provided in Table 2.

Table 2. Friction material physical parameters.

Material	Density (kg·m^{-3})	Linear Elastic Modulus (Pa)	Poisson's Ratio
Brake Disc (Q345B)	7850	2.06 × 1011	0.31
Brake Pad (Copper-Based Powder Metallurgy)	5250	5.2 × 109	0.3
Third-Body Particles (SiO_2)	2400	70,000	0.17

Given the high strain rates encountered during the friction process, determining material constants for the model presents substantial challenges. The Johnson–Cook constitutive model offers significant advantages due to its capacity to accurately characterise the work-hardening behaviour of metallic materials and effectively capture the effects of strain rate strengthening. These attributes make it especially suitable for establishing the material constants of copper-based powder metallurgy. Consequently, the Johnson–Cook constitutive model is employed to describe the mechanical properties of copper-based powder metallurgy. The mathematical expression of the model is as follows:

$$\sigma_e = \left[A + B\left(\varepsilon_e^p\right)^n\right]\left[1 + C\ln\frac{\varepsilon_e^p}{\varepsilon_o}\right]\left[1 - \left(\frac{T - T_{room}}{T_{melt} - T_{room}}\right)^m\right] \tag{3}$$

In the formula, A is the yield strength of the material, B is the strain strengthening parameter of the material, C is the empirical strain rate dependence coefficient, and the thermal softening coefficient, σ_e is the equivalent flow stress, ε_e^p is the equivalent plastic strain, $\frac{\varepsilon_e^p}{\varepsilon_o}$ is the equivalent plastic strain rate, and ε_o is the reference strain rate for the model. Its value is $e_o = 1.0S^{-1}$, T_{room} is the room temperature, and T_{melt} is the material melting temperature. $1 + C\ ln\frac{\varepsilon_e^p}{\varepsilon_o}$ and $1 - \left(\frac{T-T_{room}}{T_{melt}-T_{room}}\right)^m$, respectively, represent the strain rate effect and temperature effect.

When $\frac{\varepsilon_e^p}{\varepsilon_o}$ =1 and $T = T_{room}$, the relationship between equivalent flow stress and equivalent plastic strain is as follows:

$$\sigma_e = A + B\left(\varepsilon_e^p\right)^n \tag{4}$$

The material parameters for the Johnson–Cook constitutive model are provided in Table 3.

Table 3. Johnson–Cook constitutive model material parameters.

Constitutive Parameters	Q345B Constitutive Parameters	Copper-Based Powder Metallurgy Constitutive Parameters
A (MPa)	382	90
B (MPa)	802	292
C	0.019	0.025
n	0.401	0.31
m	0.432	1.09

In this model, the node positions of the two rough friction interfaces are defined using boundary seeds, with a uniform node spacing of 0.001 mm. An advanced meshing algorithm is utilised, which first divides the boundaries and then extends inward to generate the mesh. This method ensures consistency at the contact boundary between the particles and the matrix, effectively preventing deformed or highly distorted elements after contact. In the simulation, boundary nodes are shared between the SiO_2 frictional components and the copper matrix to improve the accuracy of local contact calculations. The element type used is CPE4R, a four-node bilinear plane strain quadrilateral element. Under these conditions, the model is meshed, as shown in Figure 7.

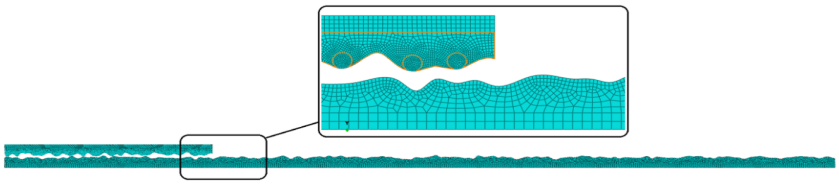


Figure 7. Mesh generation for the endogenous third-body friction contact model.

2.4. Establishment of Simulation Boundary Conditions

To simulate the braking action during the braking process, the brake pad is constrained along the X-axis, while a braking load P is applied in the Y-direction within the load-bearing area. This allows the brake pad to move freely in the Y-direction under the influence of the braking pressure, simulating the downward pressing motion. The brake disc is constrained in the Y-direction, and a braking velocity in the X-direction is applied within the load-bearing area. This induces the movement of the brake disc in the direction of the applied velocity, thereby simulating the rotational motion of the disc, as shown in Figure 8.

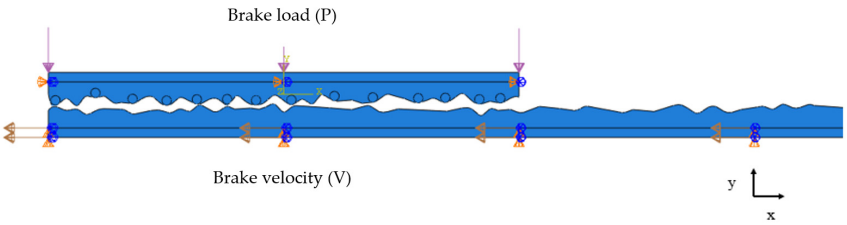


Figure 8. Boundary condition diagram of internal three-body friction contact model.

In the simulation, abrupt changes in contact conditions can directly hinder further iteration, resulting in non-convergence and significant solution errors. To address this, a loading step for braking pressure and braking velocity is incorporated into the model. The buffered loading curve is shown in Figure 9.

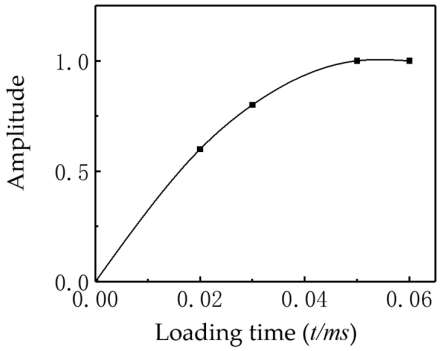


Figure 9. Load and speed loading curve.

The model is divided into two analysis steps:

Step 1: A downward load P is applied to the force-bearing layer of the brake pad. Once a stable contact is established at the rough interface, the simulation proceeds to the next step.

Step 2: A braking velocity directed to the left is applied to the force-bearing layer of the brake disc. The duration of the three-body contact process is determined by the displacement U in the X-direction under different braking velocities v, where U = 15 mm. The simulation times for various velocities are listed in Table 4.

Table 4. Analysis Step Configuration.

Analysis Step	Project Name	Variable Value
First Analysis Step	Brake Load p/MPa	3, 4, 5, 6
	Loading time t/ms	0.06
Second Analysis Step	Braking speed v/m·s^{-1}	5, 15, 25, 35
	Loading time t/ms	3, 1, 0.6, 0.429

3. Validation of the Friction System Model Containing Endogenous Third Bodies

This study utilises the MMW-1A microcomputer-controlled constant-speed friction and wear tester [37] to conduct third-body pin-on-disc friction experiments. The pin material is a copper-based powder metallurgy alloy with tin bronze as the primary matrix, while the brake disc is composed of Q345B steel. The experiments are performed under dry friction conditions with the introduction of exogenous third-body particles to explore three-body contact friction mechanisms. Selected experimental results are compared with simulation analyses of friction systems containing endogenous third bodies to evaluate the accuracy of the simulation model. Figure 10 depicts the surface wear caused by SiO_2-based third-body particles observed during the experiments. By extracting the profile lines at the frictional contact points, the experimentally measured surface height variations are compared with the simulated results to ensure consistency and validate the model.

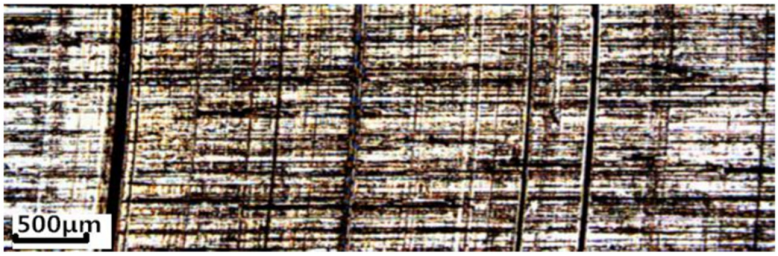


Figure 10. Surface wear by the third-body particles of SiO_2.

The braking conditions for the simulation of the friction system were set with a braking load of 5 MPa and a braking speed of 5 m/s. After the simulation concluded, the deformation in the Y-direction of the brake disc surface profile was extracted. This simulated deformation was compared with the profile changes in the brake disc before and after the dry friction experiments, as shown in Figure 11.

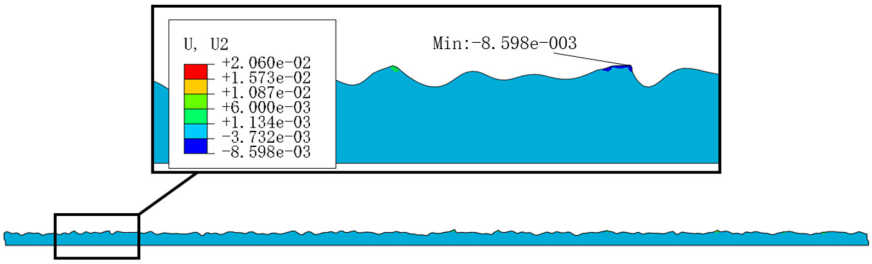


Figure 11. Y-direction deformation of brake disc interface.

As shown in Figure 12, nodes along the brake disc's surface profile, specifically from node 411 to node 1455, are selected to define an output parameter path. This path facilitates the simulation of height variations in the surface profile within the frictional region of the braking interface. By examining the contour height changes, the deformation characteristics of the brake disc under operational conditions are accurately modelled.

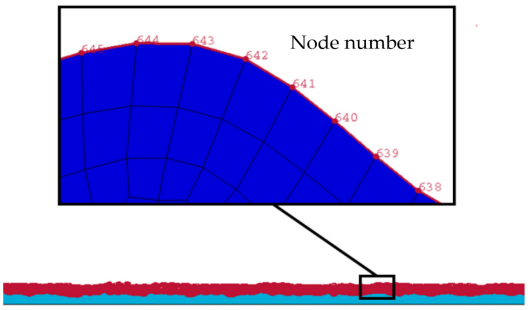


Figure 12. Contact path configuration for the brake disc interface.

Figure 13 illustrates the comparison between the simulation and experimental results. In Figure 13a, the Y-direction profile height variation curve of the brake disc is presented. The simulation indicates that the maximum tensile deformation of the friction interface profile reaches 20.6 μm, while the maximum compressive deformation is 8.6 μm, both occurring at the rising positions of the micro-asperity contours on the brake disc. Overall, the deformation range of the profile height across the friction interface lies between 6 μm and 9 μm. The tensile deformation arises from frictional interactions at the interface. When the surface micro-asperities engage with the friction interface material, the asperities, influenced by frictional forces, compress the contact material along the direction of friction. This action induces localised material sliding, leading to stretching, and, subsequently, tensile deformation. Conversely, compressive deformation is primarily attributed to the plastic deformation of the interface material under braking pressure. During this process, the braking load produces ploughing effects as the micro-asperities scratch the surface, causing localised material compression and crushing. Figure 13b displays the profile height variation curve of the brake interface obtained from experimental friction tests. The results show that the maximum groove depth on the friction interface after testing is 8.7 μm. The profile height variation observed experimentally, ranging from 6 μm to 9 μm, is consistent with the simulation results. However, certain regions exhibit deeper grooves, which can be attributed to the random detachment of hard particles within the braking

interface material. These detached particles become endogenous third bodies. With greater degrees of freedom, these particles tend to disperse, reducing the density of local third-body particles. Consequently, the embedded endogenous third-body particles amplify the scratching effect on the friction interface, resulting in deeper grooves in some areas.

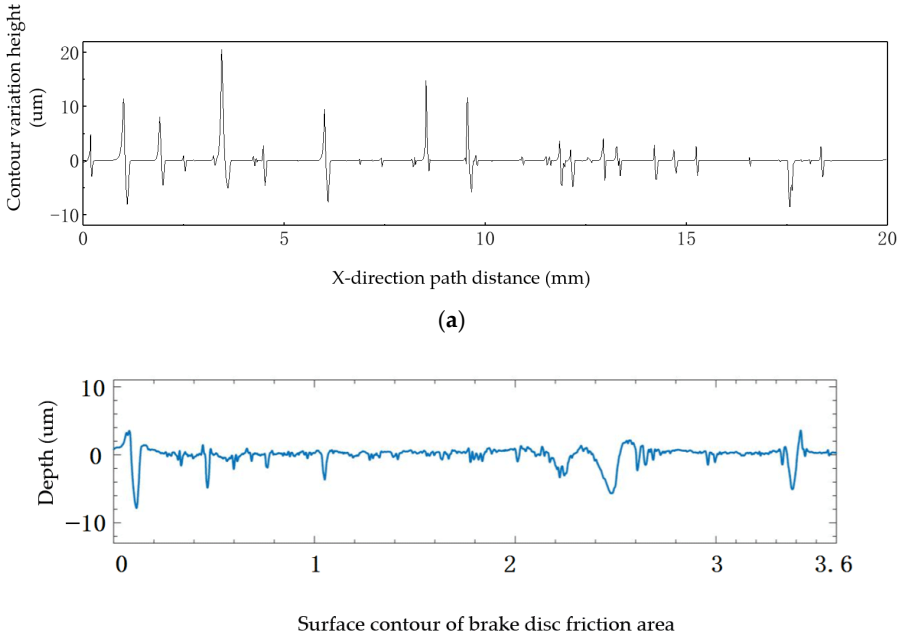


Figure 13. Comparison between simulation and experimental results. (**a**) Brake disc contour change height; and (**b**) brake disc friction area surface profile.

As shown in Figure 13, a comparison of the simulation and experimental results for the friction system containing endogenous third bodies reveals similar variation trends in the surface profile height of the braking interface on the brake disc. Both the simulation and experimental data indicate that the height variation consistently falls within the range of 6–9 μm. This agreement confirms the reliability and validity of the finite element model and its simulation results for the friction system with endogenous third bodies.

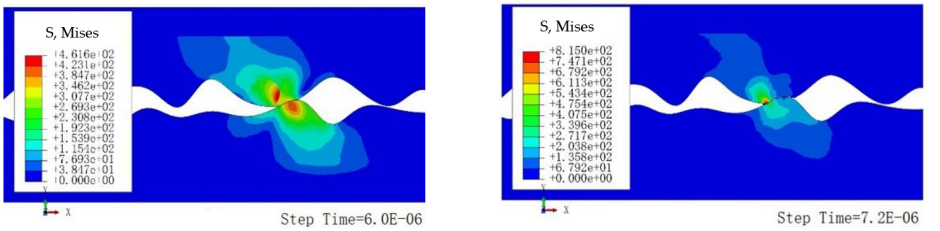
4. Analysis of the Evolutionary Behaviour of Endogenous Third Bodies During Braking

The braking process involves the interaction of two rough surfaces, where randomly distributed and uniformly scaled asperities on these interfaces collide. A subset of these asperities bears the entire applied load, resulting in significant localised contact stresses due to their curvature at the contact points. This contact process is inherently discontinuous and nonlinear. During shearing, the material releases braking-induced energy through various forms of deformation, including elastic deformation, least-plastic deformation, full plastic deformation, and eventual material failure. These interactions dynamically intensify the wear and degradation of braking materials.

4.1. Analysis of the Generation Mechanism of Endogenous Third Bodies

Figures 14 and 15 illustrate the stress and strain fields during the simulation of the generation process of endogenous hard third-body particles. The simulation assumes a braking load of 4 MPa and a braking speed of 35 m/s, focusing on the interaction, compression, and shearing between two rough interfaces at a microscopic level. Due to the sliding friction during braking, countless asperities from the brake disc and pad come into

contact simultaneously. For simplicity, this analysis selects a single pair of asperities for detailed examination.



(**a**) The simulation results were analyzed when the time was 6.0×10^{-6} s

(**b**) The simulation results were analyzed when the time was 7.2×10^{-6} s

(**c**) The simulation results were analyzed when the time was 8.1×10^{-6} s

(**d**) The simulation results were analyzed when the time was 9.6×10^{-6} s

(**e**) The simulation results were analyzed when the time was 1.1×10^{-5} s

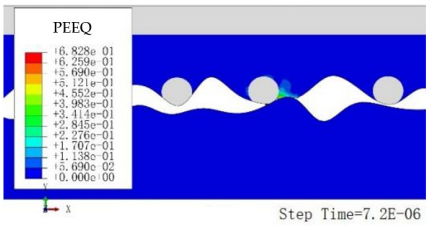
(**f**) The simulation results were analyzed when the time was 1.9×10^{-5} s

Figure 14. Stress field during the generation process of endogenous hard third-body particles.

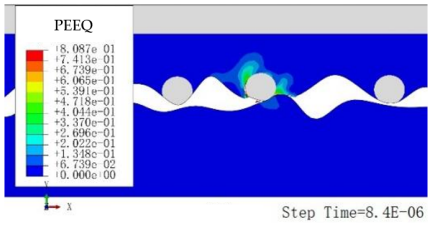
The upper plate, representing the friction surface of a copper-based powder metallurgy brake pad embedded with hard particles, slides relative to the lower plate, which models the rough surface of the brake disc. During sliding, asperities on the lower plate collide with asperities on the upper plate containing SiO_2 particles. The initial contact occurs at the edges of the copper matrix surrounding the SiO_2 asperities on the upper plate. Due to the nonlinear interaction between sliding speed and braking load, the impact induces significant stress concentrations at the contact points. At the asperity edges, the copper matrix experiences compressive stress, resulting in plastic deformation. Under the applied load, the copper matrix rapidly reaches its yield strength, after which it undergoes volumetric compression and material displacement, driving the SiO_2 particle inward. As the lower plate continues sliding, the additional copper matrix material is compressed and collapses, eventually reaching its compressive limit and fracturing. This fracture leads to the detachment of copper matrix fragments from the brake pad, forming copper-based third-body particles that exacerbate brake pad wear.

The incorporation of SiO_2 as a friction component within the copper matrix significantly enhances the friction coefficient at the braking interface. Moreover, the protruding SiO_2 particles on the friction surface induce a "ploughing" effect on the matrix material. As the sliding distance increases, the material surrounding these hard particles is rapidly worn away, diminishing its ability to retain the SiO_2 particles. Consequently, the SiO_2 particles become prone to detachment from the contact surface, leaving the copper matrix exposed as the new friction interface is in direct contact with the brake disc. This results in an

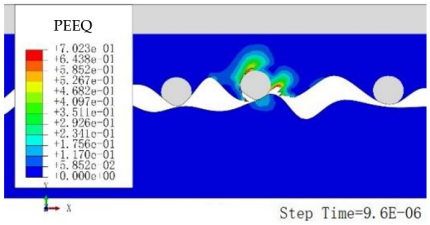
increased likelihood of localised material slippage. Such localised shearing, characterised by large strains, induces plastic deformation, which eventually leads to the formation of a layered frictional structure. This friction layer serves to protect the underlying matrix material, thereby reducing further wear and enhancing the braking system's durability.



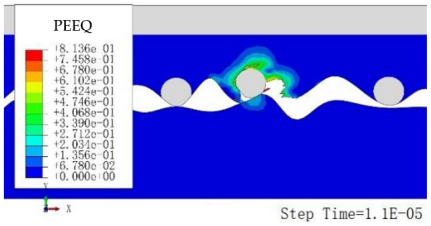
(**a**) The simulation results were analyzed when the time was 7.2×10^{-6} s



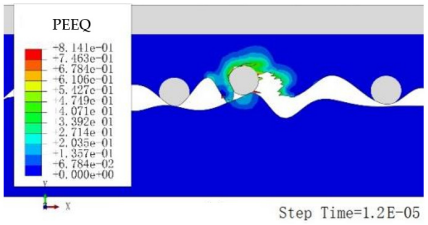
(**b**) The simulation results were analyzed when the time was 8.4×10^{-6} s



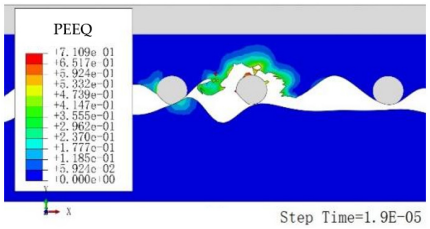
(**c**) The simulation results were analyzed when the time was 9.6×10^{-6} s



(**d**) The simulation results were analyzed when the time was 1.1×10^{-5} s



(**e**) The simulation results were analyzed when the time was 1.2×10^{-5} s



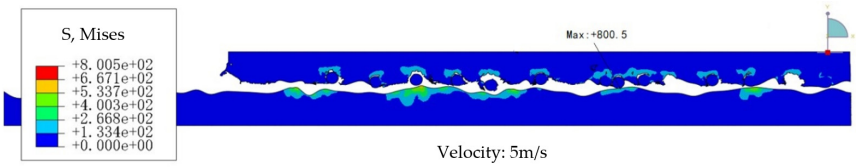
(**f**) The simulation results were analyzed when the time was 1.9×10^{-5} s

Figure 15. Strain field in the formation process of internal hard three-body particles.

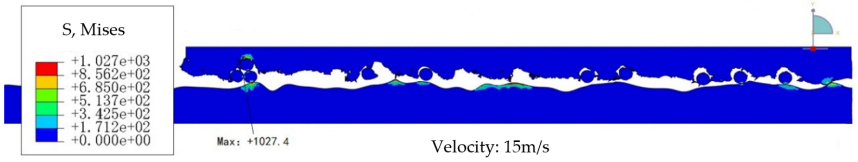
4.2. Analysis of the Evolutionary Mechanism of Endogenous Third Bodies

Figure 16 illustrates the frictional outcomes of the rough contact surfaces at the conclusion of simulations conducted under a braking load of 5 MPa, with sliding speeds of 5 m/s, 15 m/s, 25 m/s, and 35 m/s, respectively. At this stage, the upper plate consistently moves from left to right. The figure provides a detailed analysis of the motion and spatial distribution of the third-body particle clusters under varying speed conditions.

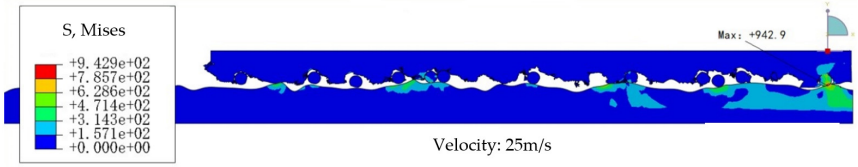
In Figure 16a,c, the maximum stress occurs at the contact points between the SiO_2 particles and the asperities of the lower plate, with stress values of 800.5 MPa and 942.9 MPa, respectively. In Figure 16b,d, the maximum stress is found at the contact points between two SiO_2 hard particles, with stress values of 1027.4 MPa and 1120.2 MPa, respectively. In Figure 16a,c, during the friction process between the two rough interfaces, the pressing and shearing forces generated by numerous asperity pairs on the rough surfaces are responsible for carrying the braking load. At any given moment, countless asperity pairs collide simultaneously, and the total contact area is the sum of each individual asperity's contact area. The maximum stress occurs when the asperity on the lower plate contacts the SiO_2 particle on the upper plate. As shown in the figures, at this moment, the number of contacting asperity pairs decreases, and the contact area between the two plates is significantly reduced. As a result, the limited contact area bears the entire braking load, leading to the maximum stress at this contact point.



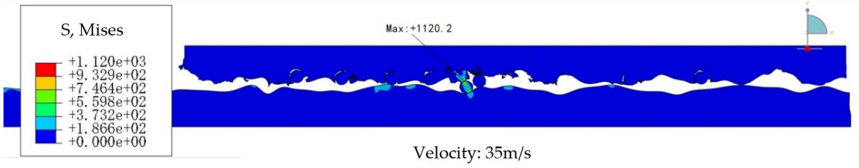
(**a**) Distribution of the endogenous third body in braking interface when the velocity is 5 m/s



(**b**) Distribution of the endogenous third body in braking interface when the velocity is 15 m/s



(**c**) Distribution of the endogenous third body in braking interface when the velocity is 25 m/s



(**d**) Distribution of the endogenous third body in braking interface when the velocity is 35 m/s

Figure 16. Distribution of the endogenous third body in braking interface with different speeds.

In Figure 16b,d, the maximum stress arises at the point of contact between two SiO_2 hard particles. At this time, both the upper and lower plates exhibit plastic deformation at the points where they contact the SiO_2 particles. The curvature at the contact point between the particles is relatively small, implying a small contact area, which results in the maximum stress value. Furthermore, between the two scenarios—contact between hard particles and the lower plate asperities—the maximum stress generated at the particle-to-particle contact is higher than that at the particle-to-asperity contact.

The stress distribution diagrams at four different speeds clearly demonstrate that the copper-based powder metallurgy material on the upper plate undergoes material failure due to collisions with the rough lower plate. Initially, the copper matrix experiences elastic deformation, elasto-plastic deformation, and failure, resulting in its separation from the matrix. Similarly, SiO_2 particles detach from the matrix, and the Q345B material undergoes both elastic and elasto-plastic deformation. Once the SiO_2 particles separate from the matrix, they remain between the rough plates, continuing to contribute to the frictional process.

The hard particles, under the influence of the frictional forces exerted by the lower plate's asperities, compress the copper matrix material and move in the direction of motion. This movement induces the elasto-plastic deformation of the surrounding copper matrix material, leading to fracture, failure, and slippage. As the particles continue to scrape the matrix, visible grooves are formed on the rough friction surface. Throughout this process, the interaction between the SiO_2 particles and the lower plate's asperities reduces the wear effect. The copper matrix supports the SiO_2 particles, increasing the contact area between the SiO_2 particles and the copper matrix. The brake pad material dissipates braking energy

through various mechanisms, including elastic deformation, elasto-plastic deformation, plastic deformation, and, eventually, matrix failure.

The distribution of copper matrix third bodies and SiO_2 material third bodies is accurately depicted in the figure. The majority of hard particles remain on the brake pad. However, due to asperity contact during sliding friction, the SiO_2 particles shift in the direction of motion and leave noticeable scraping marks in the area traversed by friction. This indicates that the incorporation of SiO_2 hard particles into copper-based powder metallurgy brake pads enhances their ability to withstand large frictional forces during braking, thus improving wear resistance. A small number of hard particles have detached from their original positions and moved along the rough interface to recessed areas, where they perform a "gap-filling" function. This refers to the phenomenon where free third bodies, under the influence of compressive shear forces during friction, embed into the recessed areas of the rough interface, filling material vacancies. The occurrence of this "gap-filling" phenomenon alters the original contour of the interface, reducing roughness and mitigating the impact of vibration-induced shocks. In certain regions, particle aggregation is observed. The hard particles push the copper matrix at the contact site to the surrounding areas, causing severe wear on the brake pad matrix. The accumulation of hard particles changes the interface profile, increasing roughness and potentially influencing the vibrational behaviour of the interface.

5. Study on the Influence of Different Braking Parameters on Friction Systems Containing Endogenous Third Bodies

5.1. The Influence of Different Braking Parameters on the Stress Field of Friction Systems

5.1.1. The Influence of Braking Speed on Contact Stress Field

Due to the inherent properties of the materials, the yield strength of the copper-based powder metallurgy material is lower than that of the brake disc material, Q345B. Consequently, the lower plate material exhibits a stronger resistance to impact. When the asperities on the upper and lower plates collide, the local material on the upper plate undergoes failure due to compressive shear forces, while the contact area of the lower plate material only experiences elasto-plastic deformation, without reaching the material failure limit. Therefore, the maximum stress values observed at the contact points on the asperities of the lower plate, representing the rough brake disc interface, are chosen as the focus of this study. Figure 17 shows the variation in the maximum stress value at the contact location of the lower plate asperity with increasing speeds, under braking loads of 3 MPa, 4 MPa, 5 MPa, and 6 MPa.

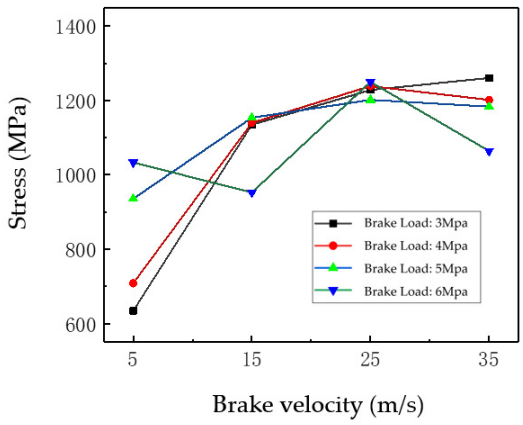


Figure 17. The maximum stress of the internal three-body friction system at different speeds.

When the braking load is less than or equal to 5 MPa, the maximum stress in the endogenous third-body friction system increases with the braking speed, though the rate of increase gradually slows. When the braking load increases to 6 MPa, the maximum stress fluctuates more significantly with the increase in braking speed. For braking loads of 3 MPa, 4 MPa, and 5 MPa, the minimum stress values occur at lower speeds, specifically at 5 m/s. As the speed increases, the maximum stress values at these speeds are 634.4 MPa, 708.7 MPa, and 939.8 MPa, respectively. For braking loads of 3 MPa, 4 MPa, and 5 MPa, the maximum stress increases gradually with speed, but this growth slows once the speed reaches 25 m/s. At a speed of 35 m/s, the maximum stress fluctuates between 1183.3 MPa and 1260.6 MPa.

When the braking load reaches 6 MPa, the maximum stress curve exhibits the greatest fluctuation, with the minimum value occurring at a braking speed of 15 m/s and the maximum value at 35 m/s. The respective maximum stresses are 952.7 MPa and 1249.8 MPa. This occurrence is due to the fact that, at a braking load of 6 MPa and a braking speed of 15 m/s, the entire friction contact process is very stable. Once the hard particles at the far-left edge of the upper plate separate from the matrix, they are directly expelled from the friction area in the direction of the lower plate's motion. The hard particles on the upper plate continue to engage in friction with the rough interface, even after separating from the matrix material. No particle aggregation occurs, and no collisions happen between particles. When the particles contact the lower plate, other asperity pairs from the plate are also in contact, creating a larger contact area for bearing the compressive shear force. No stress concentration occurs, which explains why, during the braking simulation with a 6 MPa braking load and a 15 m/s speed, the maximum stress at the contact location on the lower plate is relatively small.

5.1.2. The Influence of Braking Load on the Contact Stress Field

The maximum stress values observed on the asperities of the rough brake disc interface are selected as the focus of this study. Figure 18 shows the variation in the maximum stress values at the contact points of the lower plate asperities with increasing braking loads under braking speeds of 5 m/s, 15 m/s, 25 m/s, and 35 m/s.

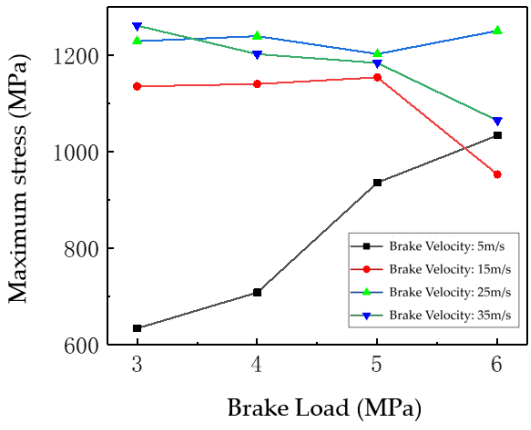


Figure 18. Maximum stress of internal three-body friction system under different loads.

From the information in the figure, it can be observed that at speeds of 5 m/s, 15 m/s, 25 m/s, and 35 m/s, the minimum stress values occur at loads of 3 MPa, 6 MPa, 5 MPa, and 6 MPa, with corresponding stress values of 634.4 MPa, 952.7 MPa, 1201.7 MPa, and 1064.1 MPa. The maximum stress values occur at loads of 6 MPa, 5 MPa, 6 MPa, and 3 MPa, with corresponding stress values of 1033.3 MPa, 1153.5 MPa, 1249.8 MPa, and 1260.6 MPa. When the braking speed is 5 m/s, the maximum stress increases steadily with increasing

braking loads. However, after the speed reaches 25 m/s, the rate of increase in maximum stress slows. At a speed of 35 m/s, the maximum stress reaches the yield limit of the brake pad material. Hard third-body particles that detach from the brake pad matrix come into direct contact with the asperities on the rough surface of the brake disc. While the contact stress does not exceed the yield limit of the brake disc material, the maximum stress occurs at the point of contact between the third-body particles and the brake disc asperities, increasing as the braking load rises.

When the braking load is 6 MPa, the maximum stress fluctuates significantly across different speeds. Under high-speed, high-load conditions, the contact state of the asperities changes. At 15 m/s and 25 m/s, the contact state is relatively stable, with an increased number of contacting pairs, and the contact area supporting the load grows, leading to smaller maximum stress values. At 35 m/s, the application of a higher braking force results in a more significant impact vibration on the braking system, degrading the contact state. The number of contacting pairs decreases, and the contact area reduces, causing an increase in the force carried per unit area, which results in higher maximum stress values.

5.2. The Influence of Different Braking Parameters on the Strain Field of Friction Systems

5.2.1. The Influence of Braking Speed on the Contact Strain Field

Figure 19 illustrates the changes in the maximum equivalent plastic strain (PEEQ) within the three-body friction system containing hard particles under different braking loads of 3 MPa, 4 MPa, 5 MPa, and 6 MPa. As the friction material undergoes elasto-plastic deformation and reaches the material failure limit, leading to material breakdown and the detachment of hard particles from the matrix, endogenous third-body particles are generated. The figure shows the variation trend of the maximum PEEQ in the three-body contact system during the process of third-body particle formation. The minimum values of the maximum equivalent plastic strain (PEEQ) occur at a braking speed of 5 m/s, with corresponding PEEQ values of 0.155, 0.329, 0.292, and 0.505 for the respective braking loads. When the braking load is 3 MPa, 4 MPa, or 6 MPa, the maximum PEEQ values are observed at a braking speed of 35 m/s, with corresponding PEEQ values of 0.904, 0.923, and 1.245. For a braking load of 5 MPa, the maximum PEEQ occurs at a speed of 25 m/s, with the corresponding PEEQ value of 1.285.

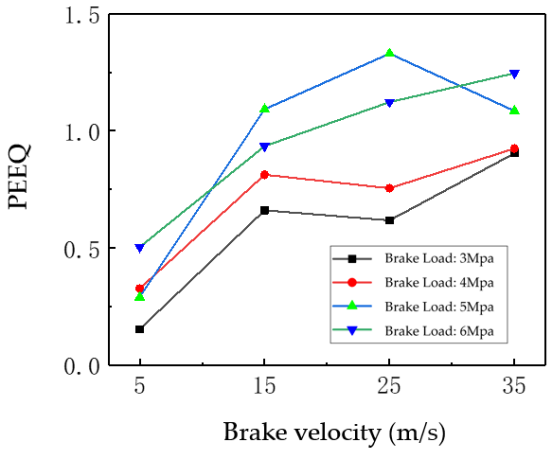


Figure 19. Maximum plastic deformation of internal three-body friction system at different speeds.

Under four different braking loads, at a speed of 5 m/s, the maximum PEEQ values are observed on the brake pad. When the braking loads are 3 MPa and 4 MPa, and the braking speed is 5 m/s, the PEEQ is located at the contact point between the hard particles on the brake pad and the copper matrix. This is also the initial point of material failure. At this stage, there is no significant plastic deformation on the brake disc, and the PEEQ

value remains relatively low. As the braking speed increases to 15 m/s, the PEEQ value also increases, and the location of the maximum PEEQ shifts from the brake pad to the brake disc. During this process, the hard particles on the brake pad directly contact the asperities on the brake disc, creating a contact similar to two half-arc surfaces. The contact area is smaller, resulting in a more intense deformation.

When the braking speed increases to 25 m/s, there is no significant increase in the PEEQ, and when the speed reaches 35 m/s, the PEEQ value shows a slight increase. When the braking load is 5 MPa, the PEEQ value increases initially with speed but then decreases, reaching the limit of the brake disc's material failure. At this stage, signs of wear on the asperities of the brake disc are observed. When the braking load is 5 MPa, as the braking speed increases, the PEEQ value shows a steady increase. When the braking speed reaches 25 m/s, the PEEQ value at the contact points of the brake disc asperities reaches the material's failure limit, and wear occurs. As the braking speed continues to increase, the PEEQ fluctuates within a certain range.

5.2.2. The Influence of Braking Load on the Contact Strain Field

Figure 20 shows the variation trend of the maximum equivalent plastic strain (PEEQ) in the exogenous third-body friction contact system under different braking speeds of 5 m/s, 15 m/s, 25 m/s, and 35 m/s. The minimum PEEQ values occur at a braking speed of 5 m/s, with corresponding PEEQ values of 0.155, 0.662, 0.619, and 0.904 for the respective braking loads. As the braking load increases at speeds of 5 m/s and 35 m/s, the PEEQ value gradually increases, with a slower increase observed at 5 m/s. When the braking speed is 15 m/s and 25 m/s, the PEEQ value initially increases and then decreases as the braking load increases.

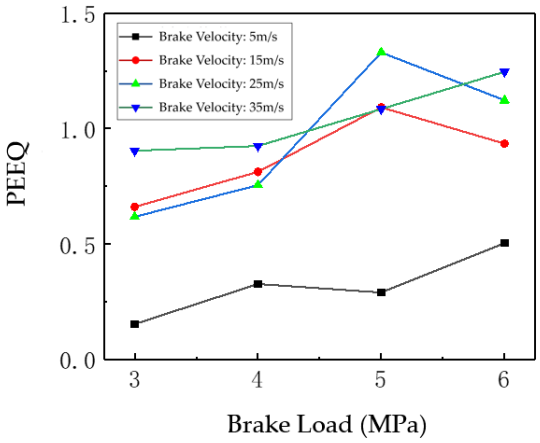


Figure 20. Maximum plastic deformation of internal three-body friction system under different loads.

When the braking speed is low, the effect of braking load on the PEEQ is minimal. This is because, at low speeds, the maximum PEEQ values are observed on the brake pad. As the braking load increases, the stability of the three-body contact system improves further. Under these conditions, the hard particles come into contact with both the brake pad matrix material and the asperities on the brake disc. The area of contact with the brake pad is relatively large, and as no material failure occurs, the load-bearing capacity remains strong. Although the contact area with the brake disc asperities is limited, the amount of plastic deformation remains small within the material's yield limit.

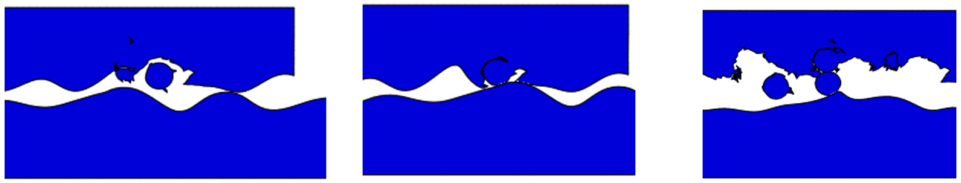
At speeds of 15 m/s, 25 m/s, and 35 m/s, the PEEQ values appear at the contact points between the hard particles and the asperities on the brake disc. In these conditions, the contact area decreases, and the contact duration becomes significantly shorter. As the

braking load increases, the PEEQ initially rises, and when the PEEQ value approaches the material failure limit, it exhibits fluctuating trends.

5.3. The Influence of Different Braking Parameters on the Vibration of the Friction System

5.3.1. The Influence of Braking Speed on Frictional Vibrations

In the friction process between two rough contact interfaces, numerous asperities on the rough surfaces interact with each other. This results in the phenomenon where the upper plate of the brake pad experiences an upward force. Figure 21 illustrates the contact scenarios of three types of endogenous third bodies with the interface, which subsequently lead to the occurrence of vibration.



(**a**) Third body detachment. (**b**) Third body movement. (**c**) Tertiary aggregation.

Figure 21. Contact between the third body and the interface.

In Figure 21a, the asperities on the lower plate directly contact the copper matrix asperities on the upper plate. Since numerous asperities on both rough surfaces are in contact simultaneously, the stress at the contact points causes plastic deformation in the upper plate asperities, although it is not enough to damage the copper matrix material. The copper matrix asperities on the upper plate are subjected to an upward load, and the upper plate asperities move along the outer contour of the lower plate asperities. Figure 21b shows the contact between the lower plate asperities and the hard particles on the upper plate. This contact generates a significant contact stress that is sufficient to cause elasto-plastic deformation in the lower plate material. The hard particles then move along the deformed contour of the lower plate asperities.

In Figure 21c, the hard particles on the rough surface of the upper plate are in contact with the lower plate asperities. After failure and wear, the hard particles detach from the matrix and, under the influence of the friction force from the lower plate, slide in the direction of motion. As they pass over the hard particles on the upper plate, they transition from aggregation to stacking. The particles then become trapped in the recesses of the lower plate and continue to move, passing over the underlying hard particles that are in direct contact with the copper matrix, and continue to participate in the friction process within the friction gap.

In summary, in all three cases, after the countless asperities on both plates are subjected to force, the upper plate asperities are lifted simultaneously as they bear the load.

To study the three-body friction vibration behaviour, a reference point P1 is selected on the brake pad, as shown in Figure 22. Since the Y-axis degree of freedom of the brake disc is fixed, it is assumed that the Y-axis displacement of the reference point P1 is equal to the vibration amplitude of the brake pad.

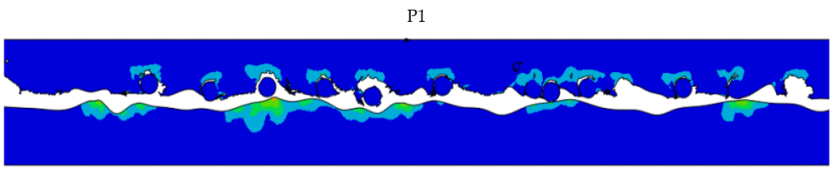


Figure 22. Schematic diagram of vibration reference point location.

Figure 23 shows the variation in the distance between two rough contact surfaces during the braking process with a braking load of 5 MPa. The speeds are set at 5 m/s, 15 m/s, 25 m/s, and 35 m/s, with the change in distance over increasing time steps. The vibration amplitude in the figure changes with every 500 time step increment (including analysis steps 70 and 430). This change is due to the simultaneous contact of numerous asperities on the rough contact surfaces at the same time. When the asperities are not damaged, the collision impact force between them is dissipated through elastic–plastic deformation. The upper and lower asperity pairs experience phenomena such as compression, scraping, and overturning, which affect the relative position of the contacting asperities.

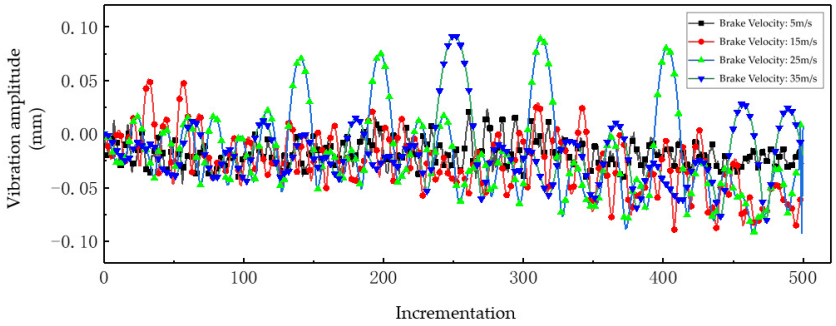


Figure 23. Vibration amplitude curve of brake pad with different braking speeds.

When the asperities are damaged, third-body particles generated by the asperity failure exist within the friction gap. These third-body particles, composed of matrix material, are compacted and aggregated by the rough interface, adhering to the recesses of the asperities. The force applied to these particles changes their shape, filling the friction gap in various forms. After the hard particles separate from the brake pad, they continue to participate in the friction process. These particles become embedded in the recesses of the brake disc asperities, continuing to scrape the brake pad material or being pressed into the brake pad matrix, where they interact with the brake disc asperities. The constantly changing three-body contact state directly affects the vibration of the brake pad. The reason for the vibration is the collective influence of the various contact states from the numerous contact points.

Figure 24 shows the variation in the average vibration amplitude of the brake pad as the braking speed increases under braking loads of 3 MPa, 4 MPa, 5 MPa, and 6 MPa. Figure 25 shows the standard deviation of the amplitude fluctuation. The average vibration amplitude increases initially and then decreases as the speed increases. At a speed of 5 m/s, the brake pad's average vibration amplitude is at its minimum, with values of 0.023 mm, 0.020 mm, 0.019 mm, and 0.017 mm for the respective braking loads. The maximum vibration amplitudes occur at 25 m/s, with values of 0.286 mm, 0.310 mm, 0.280 mm, and 0.247 mm for the respective loads.

Overall, from 5 m/s to 35 m/s, the fluctuation in the average vibration amplitude becomes more pronounced as the braking load increases. For braking loads of 3 MPa and 4 MPa, the fluctuation remains relatively stable as the speed increases. However, when the braking load increases to 5 MPa and 6 MPa, the fluctuation in the average vibration amplitude becomes more intense as the speed increases.

The maximum vibration amplitude increases initially and then decreases as the speed increases. This trend is mainly due to the fact that at lower speeds, there is enough contact time between the asperities, allowing the contact states of each asperity pair to stabilise. The simultaneous contact of multiple asperities at the same time further reduces the vibration of the brake pad. As a result, the vibration amplitude is smallest at 5 m/s, and the amplitude difference is also smaller.

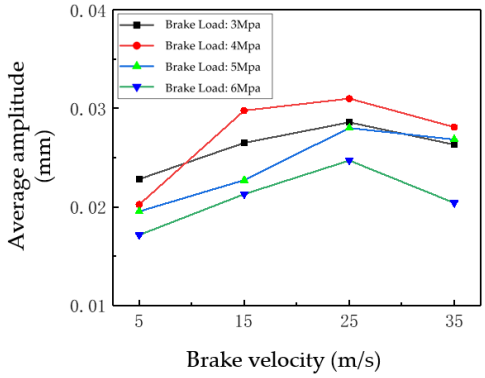


Figure 24. Relation between velocity and average vibration amplitude.

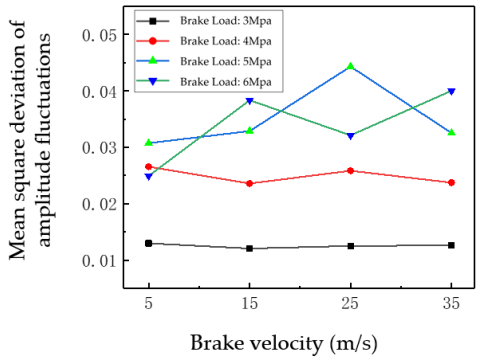


Figure 25. Mean square deviation diagram of velocity and amplitude fluctuation.

As the speed increases, the contact time between the asperity pairs decreases, intensifying the impact phenomenon and making the contact state unstable. This effect is most pronounced at 25 m/s, where the maximum amplitude is observed. This amplitude exceeds the sum of the heights of the highest asperities on the brake pad and the brake disc, indicating that significant Y-directional oscillations of the brake pad have occurred. At 35 m/s, the asperities participate in friction for a relatively shorter period, resulting in larger impacts and more pronounced damage. This leads to a higher number of third-body particles being generated. After the asperities break and produce third-body particles, their height decreases, but due to the higher speed, the vibration and impact are more significant compared to those at 15 m/s, and the maximum amplitude is somewhat reduced.

5.3.2. The Influence of Braking Load on Frictional Vibration

Figure 26 shows the variation in the distance between the two rough contact surfaces as a function of friction in the X-direction, with constant braking speed and braking loads of 3 MPa, 4 MPa, 5 MPa, and 6 MPa. From the figure, it can be observed that the vibration amplitude shows limited fluctuation during the first 0–70 steps. During the 70–250 step phase, the frequency of maximum vibration amplitude changes increases, with noticeable intense fluctuations. In the 250–500 step phase, the frequency of amplitude changes slightly decreases, though the fluctuations remain evident. This behaviour is due to the fact that in the 0–70 step range, under the action of braking load, the brake pad continually adjusts its position relative to the brake disc. The asperity morphology of both rough surfaces remains intact, and they are in an unworn state. During frictional contact, numerous asperities on both surfaces are simultaneously in contact, ensuring stable friction. In the 70–250 step range, some asperities experience stress damage, forming third-body particles that are present in the friction gap. These third-body particles exhibit strong randomness in their motion within the friction gap. As they come into contact with both rough surfaces

simultaneously, direct contact between the asperity pairs is prevented. The third-body particles bear the braking load in the friction gap and also play a role in adjusting the contact speed. As a result, the vibration amplitude of the brake pad increases due to the generation of third-body particles, which affect the contact state of the rough surfaces and lead to intensified vibration with amplitude fluctuations.

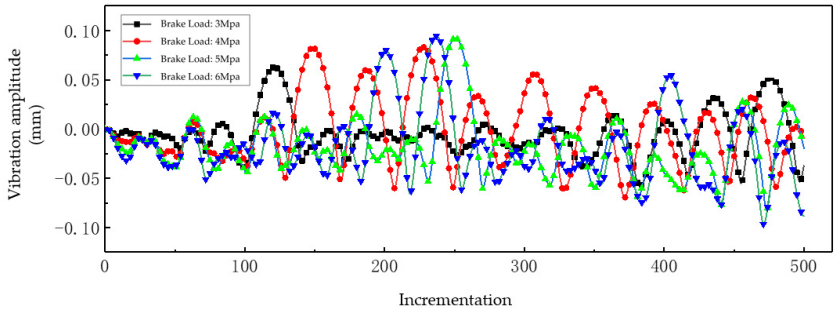


Figure 26. Variation curve of vibration amplitude of brake pads with different braking loads.

In the 250–500 step range, some of the third-body particles re-embed into the brake pad matrix material, forming new asperities that participate in the friction process and help bear the load. Other third-body particles are contained within the recesses of the asperities, reducing surface roughness peaks and decreasing the surface roughness. This leads to reduced frictional vibration fluctuations. However, due to the higher braking speed, the brake impact remains significant. At this point, the speed primarily affects the fluctuation in vibration amplitude. The change in vibration amplitude is influenced by multiple factors, and the contact state changes continuously. However, it is clear from the figure that the maximum vibration amplitude increases as the braking speed rises from 5 m/s to 35 m/s, indicating that speed is the primary factor affecting braking vibrations when the load remains constant.

Figure 27 shows the variation in the average vibration amplitude of the brake pad as the braking load increases at braking speeds of 5 m/s, 15 m/s, 25 m/s, and 35 m/s. Figure 28 shows the standard deviation of the amplitude fluctuation. At a braking speed of 5 m/s, the average vibration amplitude decreases as the braking load increases, with the maximum value occurring at 3 MPa, which is 0.023 mm. The minimum average vibration amplitude occurs at 6 MPa, with a value of 0.017 mm. At braking speeds of 15 m/s, 25 m/s, and 35 m/s, the average vibration amplitude shows an initial slow increase followed by a rapid decrease as the braking load increases. The maximum average vibration amplitude occurs at 4 MPa, with values of 0.029 mm, 0.031 mm, and 0.028 mm, respectively. The minimum average vibration amplitude occurs at 6 MPa, with values of 0.021 mm, 0.025 mm, and 0.020 mm. Overall, as the braking load increases, the vibration amplitude fluctuation of the brake pad becomes increasingly pronounced.

At a braking speed of 5 m/s, the maximum vibration amplitude of the brake pad does not change significantly. This is because, at lower speeds, the relatively higher braking load is sufficient to offset the fluctuations caused by friction, resulting in the vibration amplitude remaining relatively low and stable. However, as the speed increases to above 15 m/s, the maximum vibration amplitude of the brake pad gradually fluctuates more. At a braking load of 4 MPa, there is a noticeable increasing trend in vibration amplitude. Throughout the braking process, as the load increases, the third-body particles and asperities experience more instances of asperity overturning, leading to an unstable friction state and a significant increase in fluctuations.

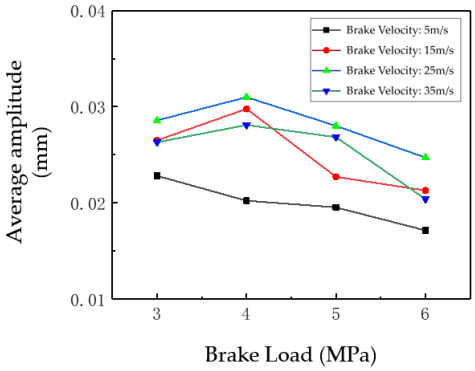


Figure 27. Relationship between load and average vibration amplitude.

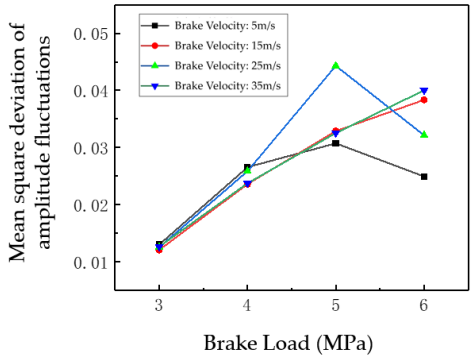


Figure 28. Mean square deviation diagram of load and amplitude fluctuation.

When the braking load increases from 4 MPa to 6 MPa, the average vibration amplitude decreases rapidly. Further increases in braking load improve the braking impact, as the braking load becomes sufficient to offset the impact forces generated during the friction process. As a result, the average vibration amplitude of the brake pad significantly decreases. However, the fluctuation behaviour at this stage becomes more complex, though still lower than at higher speeds, indicating that the frequency of the average vibration amplitude changes accelerates.

6. Conclusions

This research applies fractal theory to simulate the multi-scale roughness of friction interfaces, enabling the construction of a finite element model tailored to a braking system containing hard-particle endogenous third bodies. The validation of the model is carried out through experimental studies. The parameters for the simulation are determined from performance test results of high-power wind turbine disc brakes. This setup facilitates an in-depth analysis of the contact and friction behaviour at the rough interface between the brake pad and disc, incorporating the role of endogenous third bodies. The main findings are summarised below:

1. The roughness of the friction interface is described using the W-M fractal function, which is widely recognised for its ability to represent self-similar and multi-scale surface characteristics. A finite element model for the friction system containing endogenous third bodies is successfully established by embedding a predefined number of hard particles within the interface material. During braking, localised wear occurs in the copper-based matrix surrounding these particles, leading to their detachment and subsequent formation of endogenous third bodies. Most of these detached particles remain within the interface and participate in the friction process via a “ploughing” mechanism, causing localised displacement, material wear, and surface damage.

2. During braking, randomly distributed micro-asperities on the rough friction interface collide, creating significant stress concentrations at contact points. Hard particles embedded in the interface material add a "shearing" effect, intensifying localised material removal. As the relative sliding distance grows, the matrix surrounding the hard particles' asperities experiences accelerated wear, ultimately losing its ability to retain the particles. These detached hard particles function as endogenous third bodies. While the majority of these particles stay within the friction interface and help redistribute the load to reduce wear, a smaller portion migrates into depressions on the interface, contributing to a "gap-filling" effect that alters the surface profile, decreases roughness, and dampens vibrations. Additionally, some regions witness an aggregation of third bodies, increasing local surface roughness and potentially amplifying vibration.

3. The influence of braking parameters on the friction system containing endogenous third bodies demonstrates complex interactions. Higher braking speeds significantly intensify the impact forces between micro-asperities, leading to elevated maximum stress concentrations. Under low-speed conditions, an increase in braking load raises peak stress levels. However, at higher braking speeds, increasing the load redistributes the forces more evenly, thereby reducing stress concentrations. The strain field across the friction interface generally increases with greater braking loads and speeds, but it shows fluctuations near the material's failure threshold. As the braking speed rises from 5 m/s to 35 m/s, the system's maximum vibration amplitude first increases and then decreases, influenced by the generation, movement, and "gap-filling" actions of the endogenous third bodies. Similarly, raising the braking load from 3 MPa to 6 MPa causes the detachment and redistribution of third bodies, leading to more pronounced variations in the system's maximum vibration amplitude.

With the continuous deepening of research, the application of fractal theory in brake interface simulation will become more extensive. This article is based on the W-M classification theory and establishes a finite element model of the rough friction interface of a friction system containing an endogenous third body of hard particles during the braking process, verifying the model through experiments. Due to the limited time and resources, there are some issues that require further research: in this article, the addition of third body particles changes the original two-body contact friction state and also alters the roughness of the friction interface. The roughness of the friction changes with the action time of the third body particles, and the influence of the third body particles on the roughness of the three-body friction surface needs further exploration.

Author Contributions: Conceptualisation, L.J. and S.Z.; methodology, Y.L.; software, G.R.; validation, J.Y.; formal analysis, X.L.; investigation, L.S.; resources, S.Z. and Z.S.; data curation, L.J.; writing—original draft preparation, L.J.; writing—review and editing, Y.L.; visualisation, G.R.; supervision, Y.L. and Z.S.; project administration, Y.L.; funding acquisition, Z.S. and S.Z. All authors have read and agreed to the published version of the manuscript.

Funding: This research was funded by the General Program of National Natural Science Foundation of China, grant number 52375169.

Data Availability Statement: The data presented in this study are available upon request from the corresponding author.

Conflicts of Interest: Author Guotao Ru was employed by the company Xi'an Railway Signal Co., Ltd. The remaining authors declare that the research was conducted in the absence of any commercial or financial relationships that could be construed as a potential conflict of interest.

References

1. Zhou, J.; Li, S. Photovoltaics and Wind Power Promote Economic Development and Achieve the "Dual Carbon" Goal in Gansu Province. *Sol. Energy* **2022**, 13–19. [CrossRef]
2. Sun, R.; Xu, H.; Wu, L.; Lin, G.; Qiao, Y. Statistics on Regional Low Temperature Weather in China and Its Impact on Wind Power Generation. *Glob. Energy Internet* **2022**, *5*, 2–10.
3. Windeurope. Offshore Wind in Europe Key Trends and Statistics [EB/OL]. Available online: https://windeurope.org/about-wind/statistics/offshore/european-offshore-wind-industry-key-trends-statistics-2019/ (accessed on 9 January 2024).
4. Windeurope. Wind Energy in Europe Trends and Statistics [EB/OL]. Available online: https://windeurope.org/wp-content/uploads/files/about-wind/statistics/WindEurope-Annual-Statistics-2019.pdf (accessed on 9 January 2024).
5. Borawski, A.; Szpica, D.; Mieczkowski, G.; Awad, M.M.; Shalaby, R.M.; Sallah, M. Simulation study of the vehicle braking process with temperature-dependent coefficient of friction between brake pad and disc. *Heat Transf. Res.* **2021**, *52*, 1–11. [CrossRef]
6. Sha, Z.; Ru, G.; Yin, J.; Liu, Y.; Ma, F.; Yang, D.; Zhang, S. Research on Motion Characteristics of Single Particle Third Body in Braking Process Based on W-M Fractal Feature. *IOP Conf. Ser. Mater. Sci. Eng.* **2019**, *692*, 012011. [CrossRef]
7. Godet, M. The third-body approach: A mechanical view of wear. *Wear* **1984**, *100*, 437–452. [CrossRef]
8. Du, X.; Yang, J.; Gao, F.; Han, X.; Su, L. Mechanisms of the copper third body as an interfacial media on copper matrix friction materials with different compositions. *Ind. Lubr. Tribol.* **2021**, *73*, 1011–1018. [CrossRef]
9. Su, L.; Gao, F.; Wang, L.; Han, X.; Fu, R.; Tao, H. Iron Powder Third Body Contribution to Friction Performance of Copper-Matrix Friction Composites. *Tribol. Trans.* **2019**, *62*, 486–495. [CrossRef]
10. Su, L.; Yao, M.; Tao, H.; Yang, J.; Zhang, E.; Han, X. Tribological behavior of copper-iron particles as third body additives on copper matrix composites: Experiment link third body morphology to accommodation mechanism. *Tribol. Int.* **2024**, *191*, 109118. [CrossRef]
11. Hui, Y.; Liu, G.; Zhang, Q.; Shi, R.; Wang, C.; Wang, S.; Li, Z.; Zhang, Y. Evolution of Different Third Bodies and their Influences on the Tribological Properties of C/C-SiC Composites. *Tribol. Trans.* **2024**, *67*, 98–111. [CrossRef]
12. Tian, C.; Zhai, G.; Wu, M.; Zhou, J.; Li, Y. Analysis of wheel-rail adhesion redundancy considering the third-body medium on the rail surface. *Railw. Sci.* **2024**, *3*, 156–176. [CrossRef]
13. Gutsulyak, D.V.; Stanlake, L.J.; Qi, H. Twin disc evaluation of third body materials in the wheel/rail interface. *Tribol.-Mater. Surf. Interfaces* **2021**, *15*, 115–126. [CrossRef]
14. Flauder, S.; Langhof, N.; Krenkel, W.; Schafföner, S. Frictional performance of C/C–SiC materials at high loads: The role of composition and third-body. *Open Ceram.* **2023**, *14*, 100364. [CrossRef]
15. Khan, S.A.; Lundberg, J.; Stenström, C. The effect of third bodies on wear and friction at the wheel-rail interface. *Proc. Inst. Mech. Eng. Part F J. Rail Rapid Transit* **2022**, *236*, 662–671. [CrossRef]
16. Ciprari, S.; Ripard, V.; Saulot, A.; Massi, F. Investigation of third body role in dry contacts: Experimental procedure to dissociate the effects of substrate and interface layer on the contact pair frictional response. *Tribol. Int.* **2023**, *190*, 109047. [CrossRef]
17. Arnaud, P.; Baydoun, S.; Fouvry, S. Modeling adhesive and abrasive wear phenomena in fretting interfaces: A multiphysics approach coupling friction energy, third body and contact oxygenation concepts. *Tribol. Int.* **2021**, *161*, 107077. [CrossRef]
18. Yao, M.; Zhao, C.; Su, L.; Fu, R.; Han, X.; Gao, F. The Influence of Adding Copper and Iron Third Body on Brake Disc Temperature. *Tribol. Lett.* **2023**, *71*, 101. [CrossRef]
19. Yan, X.; Fan, C.; Wang, W.; Liu, X.; Chen, B. Experimental and simulation study of the dynamic characteristics of friction force under third-body intrusion behaviour. *Mech. Syst. Signal Process.* **2022**, *168*, 108726. [CrossRef]
20. Singla, N.; Brunel, J.F.; Mège-Revil, A.; Kasem, H.; Desplanques, Y. Experiment to Investigate the Relationship Between the Third-Body Layer and the Occurrence of Squeals in Dry Sliding Contact. *Tribol. Lett.* **2019**, *68*, 167–176. [CrossRef]
21. Goryacheva, I.; Meshcheryakova, A. Modelling of third body effect on rolling contact fatigue damage. *Mech. Res. Commun.* **2022**, *123*, 103901. [CrossRef]
22. Bouillanne, O.; Mollon, G.; Saulot, A.; Descartes, S.; Serres, N.; Chassaing, G.; Demmou, K. Wear in Progress: How Third Body Flow Controls Surface Damage. *Tribol. Lett.* **2024**, *72*, 84. [CrossRef]
23. Zhao, F.; Zhu, Z.; Yu, J.; Luo, Z.; Qi, H. Contrast Role of Third Body Layer and Hard Abrasives in the Wear Process of a TiAlSiN Hardness-Modulated Multilayer Coating: A Case Study on the Effect of Normal Load and Velocity. *Coatings* **2024**, *14*, 821. [CrossRef]
24. Garcia-Suarez, J.; Brink, T.; Molinari, J.F. Roughness Evolution Induced by Third-Body Wear. *Tribol. Lett.* **2024**, *72*, 37. [CrossRef] [PubMed]
25. Baydoun, S.; Fouvry, S.; Descartes, S. Modeling contact size effect on fretting wear: A combined contact oxygenation—Third body approach. *Wear* **2022**, *488–489*, 204168. [CrossRef]
26. Mi, X.; Bai, X.M.; Tang, P.; Xie, H.; Peng, J.F.; Zhu, M.H. The role of the third body in the fretting wear of 690 alloy. *Int. J. Mod. Phys. B* **2020**, *34*, 2050077. [CrossRef]

27. Zhu, T.; Shipway, P.; Sun, W. The dependence of wear rate on wear scar size in fretting; the role of debris (third body) expulsion from the contact. *Wear* **2019**, *440–441*, 203081. [CrossRef]
28. Liskiewicz, T.W.; Kubiak, K.J.; Mann, D.L.; Mathia, T.G. Analysis of surface roughness morphology with TRIZ methodology in automotive electrical contacts: Design against third body fretting-corrosion. *Tribol. Int.* **2020**, *143*, 106019. [CrossRef]
29. Zhang, S.; Liu, L.; Ma, X.; Zhu, G.; Tan, W. Effect of the third body layer formed at different temperature on fretting wear behavior of 316 stainless steel in the composite fretting motion of slip and impact. *Wear* **2022**, *492–493*, 204220. [CrossRef]
30. Ahmadi, A.; Sadeghi, F. A Novel Three-Dimensional Finite Element Model to Simulate Third Body Effects on Fretting Wear of Hertzian Point Contact in Partial Slip. *J. Tribol.* **2021**, *143*, 041502. [CrossRef]
31. Zhou, Y.; Mo, J.L.; Cai, Z.B.; Deng, C.G.; Peng, J.F.; Zhu, M.H. Third-body and crack behavior in white etching layer induced by sliding–rolling friction. *Tribol. Int.* **2019**, *140*, 105882. [CrossRef]
32. He, Y.; Yu, Z.; Wang, S.; Wang, J.; Feng, W.; Li, Z.; Liu, Y.; Liu, Y.; Ma, M. The Evolution of Nanoscale Third Body Layer Revealed by Graphite Structural Superlubric Contact. *Nano Lett.* **2024**, *24*, 16159–16165. [CrossRef]
33. Yan, X.; Wang, W.; Liu, X.; Zhu, G.; Zhu, L. Using a coupled FEM-DEM method to study the nonlinear phenomena of third-body behavior. *Proc. Inst. Mech. Eng. Part J J. Eng. Tribol.* **2020**, *235*, 975–988. [CrossRef]
34. Yan, X.; Wang, W.; Liu, X.; Xu, J.; Zhu, L.; Yang, B. Using FEM to study the frictional instability induced by third-body particles confined in frictional interface. *Ind. Lubr. Tribol.* **2020**, *72*, 1239–1244. [CrossRef]
35. Pham-Ba, S.; Molinari, J.F. Role of Minimum Adhesive Wear Particle Size in Third-Body Layer Properties. *Tribol. Lett.* **2023**, *71*, 98. [CrossRef]
36. Argatov, I.I.; Chai, Y.S. A self-similar model for fretting wear contact with the third body in gross slip. *Wear* **2021**, *466*, 203562. [CrossRef]
37. Cui, H. The Impact of Third-Body on the Friction and Wear Characteristics of Wind Turbine Brake Friction Pairs. Master's Thesis, Dalian Jiaotong University, Dalian, China, 2019.

Disclaimer/Publisher's Note: The statements, opinions and data contained in all publications are solely those of the individual author(s) and contributor(s) and not of MDPI and/or the editor(s). MDPI and/or the editor(s) disclaim responsibility for any injury to people or property resulting from any ideas, methods, instructions or products referred to in the content.